Invited Articles

Shape formation in interfacial flows

P.-T. Brun *

Department of Chemical and Biological Engineering, Princeton University, Princeton, New Jersey 08540, USA

(Received 12 June 2024; accepted 11 September 2024; published 4 November 2024)

Interfacial fluid dynamics has a rich history of systematically exploring intricate flows studied for their technological and heuristic value. Surface tension typically forms exceptionally smooth shapes, yet the same cohesive forces can precipitate the rearrangement and breakup of liquids through a wealth of hydrodynamic instabilities. This article summarizes, albeit nonexhaustively, recent efforts to tame interfacial flows in solidifying polymer melts. The article tackles both these flows' stable and unstable limits and focuses on the fundamental challenges and opportunities of harnessing interfacial effects to shape soft materials.

DOI: 10.1103/PhysRevFluids.9.110501

I. INTRODUCTION

Patterns are ubiquitous in nature, with examples spanning the intricate fractals of snowflakes, the rhythmic pulsations of heartbeats, bifurcations in the veins of a leaf, and spiral formations of galaxies. While these patterns offer a glimpse into the beauty and complexity of our world, they often play a practical role, too; for instance, materials in nature typically comprise intricate patterns whose hierarchical arrangements imbue them with enhanced properties. Latticelike patterned structures in trabecular bones are lightweight while providing a load-bearing structural behavior [1]. Superhydrophobicity in lotus leaves is achieved with hierarchical structures comprising a pattern of microscopic cones of epidermal cells and covered by nanometric wax tubules [2]. Similarly, patterns at the nano- and microscale enable the manipulation of electromagnetic waves, e.g., leading to the iridescence of certain butterflies [3] and the color-changing capabilities of chameleon skins [4]. In recent years we have witnessed the emergence of various engineering fields aiming to build materials with similar enhanced capabilities, the so-called metamaterials. Initially developed in optics [5] and acoustics [6], these materials were later ported to solid mechanics [7,8]. While such materials have now been widely demonstrated at the laboratory scale, their deployment in our daily lives remains challenging. Building metamaterials with top-down and bottom-up methods presents several challenges due to the intricacies of designing and fabricating structures with precise control over their geometry [9]. For example, two-photon lithography requires specialized equipment and expertise, and achieving high-resolution features over large areas can be costly and time consuming. As such, the idea of producing patterned metamaterials for large-scale applications, e.g., in construction, mostly remains in science fiction. This limitation provides a tremendous opportunity for fluid dynamics [10,11]. This article aims to showcase, albeit not exhaustively, how pattern-forming instabilities and other interfacial flows can facilitate the creation of functional materials with intricate structures. The motivation behind this endeavor stems from the observation that natural patterns often emerge spontaneously without the need for deliberate control by an operator [12]. Consequently, such patterns can manifest over vast scales; consider the ripples in the sand beneath the ocean's surface [13] or the cracks that develop in drying mud or cooling volcanic

*Contact author: pierrethomas.brun@gmail.com

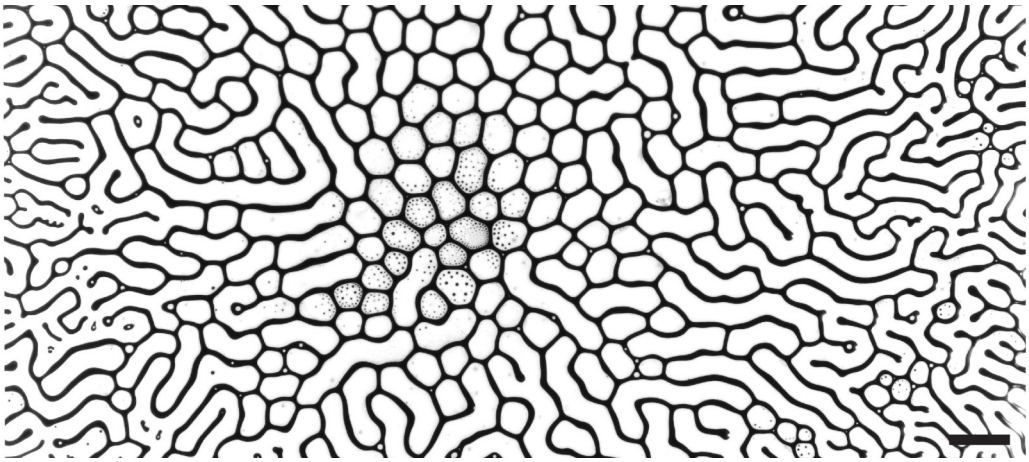

FIG. 1. Mixing paint and ferrofluids yields complex labyrinthlike patterns when a magnet is approached to the mixture (see Ref. [16] for details on the Rosensweig instability). Scale bar is 100 μm in length.

lava [14]. Moreover, these patterns can emerge effortlessly at small scales, as one can notice while contemplating the dewdrops adorning spiderwebs [15], or else, by mixing paint with ferrofluids [16] (see Fig. 1). The latter examples highlight the intrinsic ability of fluid flows to generate complexity without inputting explicit directives dictating the distribution of matter. Harnessing these flows for materials design represents a departure from traditional fabrication methods, which often rely on meticulous planning and precise control at every stage. Instead, we embrace the spontaneity and adaptability inherent to fluid dynamics, enabling complex architectures and properties to emerge and offering a fertile ground for exploration. This article is divided into two sections: the first explores instabilities, while the second considers the stable limit of thin-film flows.

II. RAYLEIGH-TAYLOR INSTABILITY IN THIN FILMS

A. Stability analysis

The Rayleigh-Taylor instability or RTI describes the process that occurs when a dense fluid sits on top of a lighter one in a given acceleration field [17]. This instability causes the mixing of stratified interfaces across a broad spectrum of atmospheric, oceanic, geophysical, and astrophysical settings [18]. This instability can also be observed in thin liquid coatings applied on the underside of a substrate [19], where the instability typically manifests itself by forming an array of droplets [see Fig. 2(a)]. Here, we consider this thin film limit and will discuss the case where the substrate is a flat plate, and the acceleration comes from gravity, as well as the case where the coating is applied to a rotating cylinder [20]. In both cases, the instability is mediated by the accelerating field a, which pulls the liquid away from the substrate and is resisted by surface tension γ, which opposes any surface area increase. Energy arguments alone tell us that any large drop can grow [21]. The threshold is $2\pi\ell_c$, where $\ell_c = \sqrt{\gamma/(\rho a)}$ is the capillary length. Yet, the instability is evidently more selective (see the regularity of the drops in Fig. 2). We must study the dynamics at play to rationalize the regular patterns we observe. To this end, we investigate the stability of the uniform base solution with thickness h_0 to periodic perturbations $h = h_0(1 + \epsilon\cos(\lambda x))$ where λ is the wavelength of the perturbation and $\epsilon \ll 1$ an arbitrarily small parameter. The rationale for seeking periodic perturbations is that any defect in the coating, bump, valley, or otherwise, can be decomposed into Fourier modes, whose evolution is independent of each other at the linear order. Since we operate near the equilibrium, we seek solutions to the temporal evolution of this perturbation of the type $h \propto \exp(-i\omega t)$. We write the lubrication equation anticipating that the coating thickness h_0 is much smaller than the length scale of the problem λ to find the dispersion

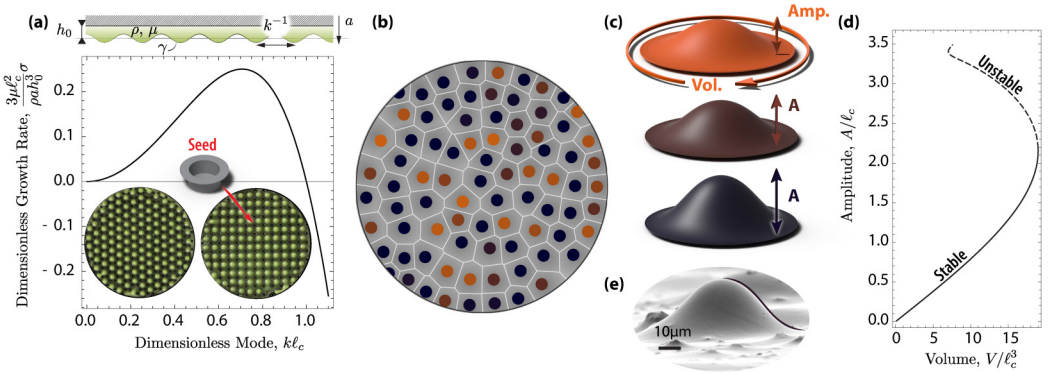

FIG. 2. (a) Plot of the dispersion relation in Eq. (1) describing the RTI of a thin film with thickness h_0 coated on the underside of subsrate. The top shows the configuration on a circular plate, and the inset shows the drop patterns obtained by forcing the system with lattices of seeds. These patterns contrast with (b), the drop pattern formed after one coating is applied to a flat plate without seed. (c) These pendant drops with increasing amplitude and volume belong to a family of solutions of the three-dimensional Young-Laplace equation in 3D (d). (e) Microscopic droplet formed using centrifugal acceleration [20]—black line indicates the theoretical prediction.

relation of the instability [22]:

$$\omega(k) = i\frac{\rho a h_0^3}{3\mu}\left(k^2 - \ell_c^2 k^4\right), \tag{1}$$

where μ is the liquid viscosity, ρ its density, $\ell_c = \sqrt{\gamma/(\rho a)}$ is the capillary length, and ω and $k = 2\pi/\lambda$ are the instability's frequency and wavenumber, respectively. The imaginary part of ω is the growth rate of the instability, σ. Here, long wavelengths are unstable ($\sigma > 0$), while short wavelengths $k > 1/\ell_c$ are stable ($\sigma < 0$). The most unstable mode of the instability is $k_m = 1/(\sqrt{2}\ell_c)$ corresponding to the wavelength

$$\lambda_{\mathrm{m}} = 2\pi\sqrt{2}\ell_c. \tag{2}$$

Equation (2) implies that the distance between drops formed by the instability should match λ_{m} [19,20]. Before examining how this insight holds in experiments, we can make a few immediate comments on the nature of Eqs. (1) and (2).

First, the fluid's viscosity and initial thickness affect the temporal nature of the growth rate but do not set the value of the most unstable mode. Two coatings of the same fluid with different values of h_0 or two coatings of different viscosities with the same surface tension evolve toward the same mode. However, the growth rate is very sensitive in the value of h_0 as it is cubed in Eq. (1). Slight differences in thickness could lead to very different dynamics.

Second, Eq. (1) is, by definition, flat near its maximum. There is a neighborhood of values around λ_{m} whose growth rate is approximately equal to $\sigma(\lambda_{\mathrm{m}})$.

Third, Eq. (1) has a real part when the base flow has a finite speed, as would be the case if the coating were applied to a plate inclined with angle α. In such a case, the instability would develop locally if and only if the time scale of the instability $1/\sigma(\lambda_{\mathrm{m}})$ is less than the time scale of the flow $\lambda_{\mathrm{m}}/(\rho a \cos(\alpha) h_0^2/\mu)$ [22,23]. The RTI can be suppressed if the slope is large enough. The instability is then said to be convectively unstable [22].

Fourth, Eq. (2) indicates that λ_{m} varies inversely proportionally to $\sqrt{a}$. It is, thus, theoretically possible to control the size of the droplets formed by the instability by modulating the amplitude of the acceleration field, so long that the physics of the problem is not altered (as would be if considering Van der Waals forces and other effects relevant when continuum mechanics breaks

down). Accelerations 10^4–10^5 times gravity are routinely accessible to centrifuges, so droplets 100–1000 times smaller than those formed in gravity can be formed [20].

B. Experiments and discussion

In recent years, experiments have been carried out on thin films coated on the underside of a plate [19,20,22], the underside of a cylinder [24,25] or a sphere [26] (not rotated), or the outside of a cylinder [20,27]. These works establish that the RTI can be suppressed via the geometry of the substrate. There also exists literature on active strategies deployed to counteract the effects of the RTI [28], which we do not attempt to discuss here. Instead, we focus on experimental efforts to harness the RTI, starting from the case of coatings applied on the underside of a flat plate. As predicted by Eq. (1), we find that perturbations grow exponentially to form droplets whose mean distance is well captured by Eq. (2). However, even in cases where considerable efforts are made to start with a uniform coating, the drop population is somehow polydisperse [19,20,29] [see Fig. 2(b)]. This dispersity manifests itself in two equivalent ways. The tiling defined from the location of the drops' apex comprises hexagons, pentagons, and heptagons, thus deviating from a hexagonal ideal. Each drop thus grows by pulling fluid from pools of different volumes and, thus, can reach a broad range of sizes [Fig. 2(c)]. The initial thickness h_0 can be chosen sufficiently small for the drop growth to be interrupted before dripping occurs [20]. In the long run, however, the irregularity of the lattice eventually causes neighboring droplets to flow toward each other [30,31], merge, and likely drip, thereby reducing the number of drops on the plate (increasing the apparent mean wavelength).

From a formal standpoint, polydispersity is due to defects in the coating, from which the instability grows. Those defects are typically present at the contact line. We witness drops forming at the edge of the coating first and then subsequently invading the sample. This propagation results in complex dynamics where disclinations and other rearrangements occur. Similar dynamics occur if significant defects are present across the sample. The instability propagates radially from these points, and axisymmetry eventually vanishes when such a front meets another front or a boundary [19]. In any case, defects drive pattern formation. Based on this observation, we have proposed using carefully crafted seeds to control and tune these patterns [20]. In those experiments, small cavities are edged into the sample before coating [20] [see inset of Fig. 2(a)]. By design, the spacing between seeds matches the most unstable mode λ_{m} defined in Eq. (2). We observe that the drops form away from these seeds. The drops are centered on the vertices of the Voronoi mesh built based on the seeds' location. As such, a triangular lattice of seeds will lead to a triangular lattice of drops, while a square lattice of drops can be formed using a square lattice of seeds [see Fig. 2(a)]. Owing to the regularity of the seeds' lattice, the drops grow with access to the same volume and thus reach a uniform amplitude across the sample. Similar results can be produced using thin cables instead of cavities [19]. In this case, the cable is deposited on top of the surface before coating, yielding a bump and causing the instability to develop on top of the cable first. Crossing two cables defines an angle that can be used to dictate the symmetry of the pattern. An angle of 90° will give a square lattice, while an angle of 60° will create a hexagonal arrangement. This approach is particularly interesting as it, allows for driving pattern formation with fewer seeds relative to the number of droplets.

Microscopic droplets can be formed leveraging Eq. (2), since $\ell_c \propto a^{-1}$ with $a = R\Omega^2$ in the case of coatings applied to rotating cylinders [20] (radius R, speed Ω). After the droplets grow exponentially, their amplitude saturates due to lack of liquid. The droplet growth has virtually exhausted the volume of liquid initially coated on the substrate. This limit has been thoroughly studied in Refs. [30,31], demonstrating that such drops are pendant drops sitting on very thin and nonuniform films. This situation is unstable, as the drops will eventually slide toward each other. However, within short time scales, any perturbation to the drop relaxes much before any fluid from the film in the regions could flow. Therefore, we can integrate their shape using the axisymmetric Young-Laplace equation [20]. Integrating this set of equations provides a family of shapes with various amplitudes A and volumes V [see some examples in Fig. 2(c)]. A critical volume exists beyond which no static equilibrium exists [see Fig. 2(d)]; the drop will then pinch off. Two

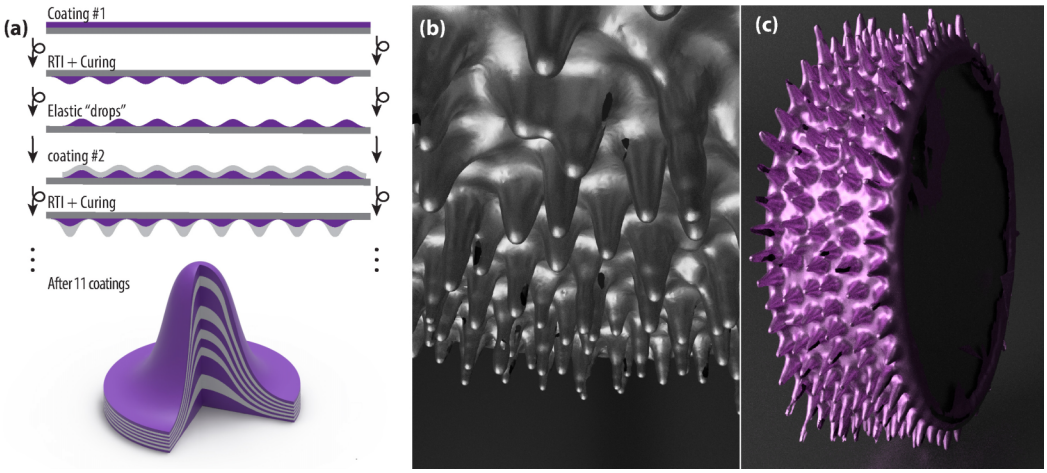

FIG. 3. Schematic of the experiment in Ref. [29], where sequential coatings of polymers are applied to a substrate. Three-dimensional rendering of the structure that forms after applying 11 coatings. (b) shows a rendering of these coatings on a flat plate (drop spacing is roughly 1cm), and (c) shows the same structures on a rotating cylinder (38 mm radius).

amplitudes A can be found for a range of volumes, but only the shorter drop corresponds to a stable shape, so we have $A \lesssim 2\ell_c$. Remarkably, the shape of macroscopic and microscopic droplets alike can be predicted following this approach [see Fig. 2(e)]. The long-term behavior of these drops has been studied on flat [30] and slanted substrates [31]. They are unstable and will spontaneously move across the substrate with speed U defined by

$$\mathrm{Ca}^{2/3} = 0.0553 A h_\mathrm{f}/\ell_c^2, \tag{3}$$

where h_f denotes the thickness of the film lubricating the drop motion and Ca is the capillary number $\mathrm{Ca} = \mu U/\gamma$. This result can be obtained using a Landau-Levich-like argument to study the drop's motion [31].

In the case of Fig. 2, this long-term dynamics limit is never attained. The liquid employed is a curable elastomer whose viscosity diverges in finite time and can be described as

$$\mu = \frac{\mu_0}{(1 - t/\tau_c)^2}, \tag{4}$$

with μ_0 the initial value of the viscosity (a few Pa.s), and τ_c is the curing time (10 min or so). The rheology in Eq. (4) is such that the liquid can be considered Newtonian with $\mu \simeq \mu_0$ throughout the growth of the drops. However, curing occurs sufficiently fast for the drops to be frozen before they move, merge, and drip, thereby allowing the fabrication of complex solids. Curing also allows for multiple coatings to be realized on top of one another [29] as described next.

We work in the limit where the time between coatings is sufficient to allow complete elastomer curing before a new layer is applied. This process gives rise to vertical structures that resemble stalactites [29] (see Fig. 3). Each layer of these elastomeric formations has a structure similar to that discussed for single coatings on flat plates. In fact, after N coatings, we find that the coating $N + 1$ gives rise to pendant drops, which form on top of the previous ones. These drops are separated from a distance λ_m [predicted in Eq. (2)]. The accumulation process is stochastic: excess amounts of liquids are applied to ensure the sample is fully coated and most of it drips. Predicting how much

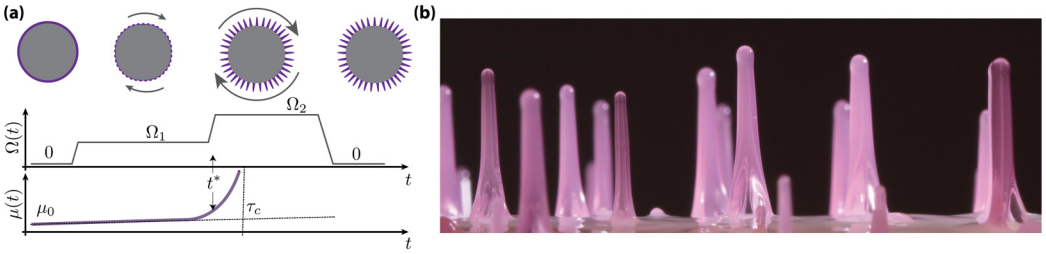

FIG. 4. (a) Working principle of the experiment in Ref. [27] where a cylinder is rotated at different speeds Ω while the coating applied to its surface is curing as denoted by the variation of its viscosity $\mu(t)$. τ_c denotes the curing time. (b) Photopraph of the structures obtained following this approach. The sample is accelerated at about 100 times the acceleration of gravity while curing.

fluid remains trapped is virtually impossible. Yet, we find that the mean drop amplitude obeys

$$\frac{1}{N_d}\sum_{i=0}^{N_d} A_i \simeq 0.8\,\ell_c, \tag{5}$$

with $N_d \gg 10$, the number of drops, and A_i their individual amplitude. This information alone allows us to estimate the average height of the structures after N coatings, $H \simeq N \times 0.8\,\ell_c$. The films that connect on these drops have a uniform thickness [see Fig. 3(a)], which ultimately sets the conical geometry of the structure (they have an opening angle of roughly 10° [29]). This methodology yields a forest of slender structures [see Figs. 3(b) and 3(c)] whose deformability and controlled polydispersity can be used to build rudimentary force sensors [29].

In the above-mentioned examples, the fluid's rheology plays a minimal role. By design, our polymers were chosen so that Newtonian predictions would hold while allowing the structures to freeze before any long-time effect would take place [20]. However, it is possible to leverage the rheology further by changing how the experiment is driven, e.g., by modifying the value of the acceleration field a throughout the curing process [27] [see Fig. 4(a)]. To this end, we focus on coatings applied to rotating cylinders and change the rotation speed of the cylinder from Ω_1 to $\Omega_2 > \Omega_1$ at a time t^* that allows drops to develop before changing the rotation speed [$t^* \gg \mu\ell_c^4/(\gamma h_0^3)$] and before the polymer is fully cured ($t^* \leqslant \tau_c$). For the sake of simplicity, we chose $t^* = \tau_g$, the gelation time of the polymer defined as the time when storage and loss modulus are equal. Prior to t^*, the drops form and saturate to a static shape. As the rotation speed Ω increases, these drops deform elastically to form hairlike structures (see Fig. 4). Starting from an amplitude A these structures reach a size λA with

$$\lambda = 1 + \frac{\beta}{3}\frac{\rho R\left(\Omega_2^2 - \Omega_1^2\right)A}{G} \tag{6}$$

with G the shear modulus ($G \simeq 200$ Pa with our polymers), and $\beta \simeq 0.3$ a numerical factor representing the drop's shape [27]. These structures form rapidly after Ω_2 is imposed, so $G = G'(\tau_g)$ is a good approximation. These stressed shapes further polymerize and $G'(\tau_c) \gg G'(\tau_g)$, with τ_c the curing time (Fig. 4). Curing thus defines a new reference state that remains underformed when all rotations are stopped and $\Omega = 0$. The linear relation in Eq. (6) is valid in the limit of small enough differences between Ω_2 and Ω_1 [$\frac{\rho R(\Omega_2^2-\Omega_1^2)A}{G} < 5$]. Note that Eq. (6) indicates that initial differences in amplitude are amplified after the change in acceleration. The distribution of amplitudes of the drops tends to spread when hairs are formed. This spreading can go beyond what Eq. (6) predicts [27] when other nonlinear effects come into play, e.g., delaminationlike effects break the axisymmetry of the hairs [see Fig. 4(b)].

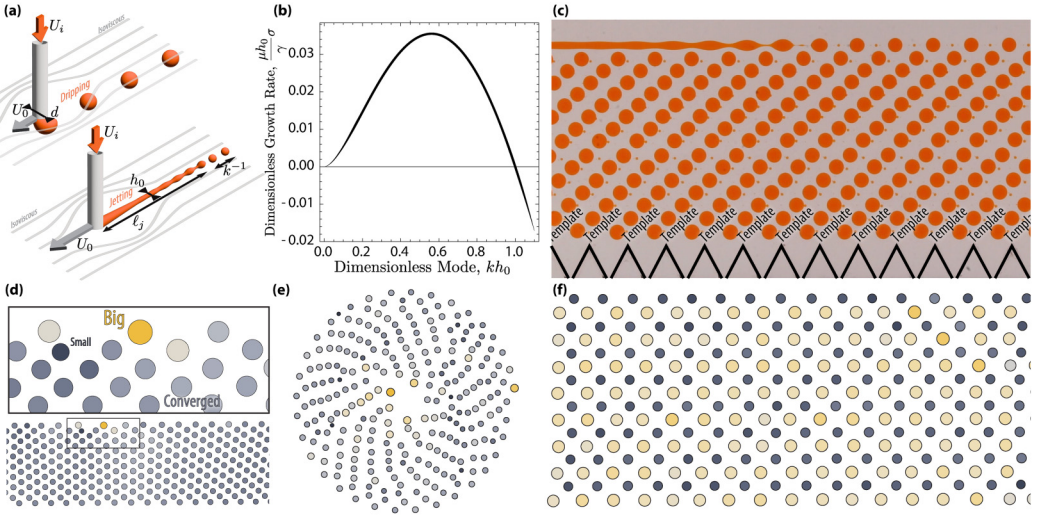

FIG. 5. (a) Schematic of the experiment showing an orange liquid injected at speed U_i in a bath of another immiscible liquid (transparent). The syringe is dragged into the bath at speed U_0, causing dripping (top) or jetting (bottom). The jet of length ℓ_j thins to a diameter h_0 before breaking into drops separated by a distance $\lambda = k^{-1}$. (b) Dispersion relation in Eq. (7). (c) Photograph of a droplet lattice obtained via templating. (d) The inset shows the drop lattice obtained when printing successive threads next to each other following Refs. [40,41] (first line on top). Colors from blue to yellow tones code for increasing droplet size. (e) Drop lattice corresponding to a spiral printing path. (f) Lattice with drops of different sizes obtained by locking [41]. All droplets in the figure are a few mm in diameter.

III. RAYLEIGH-PLATEAU INSTABILITY OF SUBMERGED VISCOUS JETS

The Rayleigh-Plateau instability or RPI describes the breakup of a liquid thread into a collection of drops. Unlike the Rayleigh-Taylor instability, which is resisted by surface tension, the RPI is driven by interfacial effects, aiming to lower the surface energy of the jet. This instability is very common, breaking the stream of water from a tap, and has been extensively studied [32]. Here, we focus on the case where the jet is submerged into another immiscible phase. This situation is common in microfluidic systems, and the RPI's ability to produce regular droplets is the basis of many laboratory-on-the-chip techniques [33,34]. While extreme care is usually taken to produce monodisperse droplets in these applications [35], little can be done to organize them afterward. Removing the continuous phase surrounding the drops yields hexagonal-packed suspensions [36], but other patterns are usually unattainable. The subsequent sections build toward overcoming this limitation.

A. Stability analysis

We focus on the case where a cylinder with viscosity μ and radius h_0 is submerged into an isoviscous and immiscible liquid [see Fig. 5(a)]. In this limit, the growth rate of periodic perturbations can be elegantly calculated [37]:

$$\sigma(k) = \frac{\gamma}{\mu h_0}\left(1 - h_0^2 k^2\right)\left(I_1(h_0k)K_1(h_0k) + \frac{h_0 k}{2}\left(I_1(h_0k)K_0(h_0k) - I_0(h_0k)K_1(h_0k)\right)\right), \qquad (7)$$

where γ is the interfacial tension and I_i and K_i are modified Bessel functions. The expression in Eq. (7) is a particular case of the more generic relation in Ref. [38]. With Eq. (7), we recover the classic cutoff where $\sigma > 0$ for $kh_0 < 1$, i.e., the thread is unstable to perturbation with wavelengths

greater than its radius. This result can be worked out by considering energy arguments. However, energy alone would suggest that $k = 0$ is most favorable. Dynamics forbids this limit and suggests that $k_m h_0 \simeq 0.56$ is the most unstable mode. A few comments can be made about this result.

First, and per the definition of a local maximum, σ is locally flat near the most unstable mode. Consequently, in the vicinity of k_m, there is a continuous range of modes with a growth rate approximatively equal to the max of σ, denoted σ_m. The value of σ_m is small compared to unity ($\sigma_m \simeq 0.04 \frac{\gamma}{\mu h_0}$), a detail that will have practical consequences in the next section.

Second, the growth rate is inversely proportional to h_0, which is unknown *a priori*. For instance, when a jet is accelerated by gravity or by drag, the value of h_0 decreases following mass conservation [39].

Third, the jet's breakup can be delayed or even canceled. Think of a tap for which, at a very small flow rate, water drips from the faucet (this is not the RPI), while for an intermediate flow rate, a jet will form and break midair. Finally, a higher flow rate stabilizes the jet, which remains intact until it impinges on the bottom of the sink. We discuss this situation quantitatively in the next section.

B. Experiments and discussion

We are considering the case where glycerol is extruded from a needle with diameter d at speed U_i. At the same time, the needle is dragged into a bath of another immiscible liquid at speed U_0 [Fig. 5(a)]. Both liquids have the same viscosity of $\mu = 1$Pa.s, and their interfacial tension is $\gamma = 28\,$mN/m. The bath can be silicon oil or silicon-based polymer (Polyvinyl dimethyl siloxane). In the latter, curing is negligible throughout the experiment and occurs at long times, allowing for capturing the suspension of glycerol droplets and freezing their position in place [40–42]. This process forms elastic slabs that contain regularly spaced liquid inclusions. The overall goal of this section is to rationalize the physics at play in setting the size and position of these inclusions and provide design guidelines for tailoring these properties.

Our jet can break following two regimes [see Fig. 5(a)]. In the first regime, called jetting, a jet with length ℓ_j forms and thins so that $h_0 = d(U_i/U_0)^{1/2}$, following mass conservation. We operate with $U_0 \geqslant U_i$, so that $h_0 < d$. This jet eventually breaks following the dispersion relation in Eq. (7). This relation has two practical consequences. First, the mean distance between droplets (ignoring satellite drops [43]) is $\lambda = 2\pi/k_m$, where k_m is the most unstable mode ($\lambda \simeq 10 h_0$). Second, the jet length can be approximated by $\ell_j \simeq U_i \sigma(k_m)^{-1}$. Recalling that $\sigma \propto h_0^{-1}$ and that $h_0 \propto (U_i/U_0)^{1/2}$, we find that

$$\ell_j \simeq \frac{\mu d}{\gamma} \sqrt{U_0 U_i}. \tag{8}$$

Equation (8) indicates that the length of the jet decreases when the product $U_0 U_i$ decreases and can thus become vanishingly small.

There is a second regime for drop formation, called dripping [40], where drops form directly at the nozzle. This breakup mode does not obey a dispersion relation; instead, the droplet size can be directly derived from a force balance [33]. A drop with radius R detaches when the viscous drag acting on it, $\mu U_0 R$, exceeds interfacial adhesion forces γR, yielding

$$R \propto \gamma d / U_0. \tag{9}$$

In Ref. [40], we argue that the transition from jetting to dripping occurs when the jet length ℓ_j equals the dripping drop size R in Eq. (9). Equating Eqs. (8) and (9) yields a transition when

$$\mathrm{Ca}_{\mathrm{in}} = \mathrm{Ca}_{\mathrm{out}}^{-3}, \tag{10}$$

where $\mathrm{Ca}_{\mathrm{in}} = \mu U_i/\gamma$ and $\mathrm{Ca}_{\mathrm{out}} = \mu U_0/\gamma$ are the inside and outside capillary number, respectively. Equation (10) applies when inertia effects are negligible [34]. At any rate, Eq. (10) allows us to find parameters to ensure we are operating in the jetting regime. While dripping produces regular

droplets, these drops are larger than the nozzle diameter. Instead, we rely on jetting and drag the injection needle fast enough to produce thin jets and thus form small droplets. Recall that the wavelength of the instability is proportional to the jet width, which, in turn, is proportional to $U_0^{-1/2}$. Increasing U_0 thus decreases the size of the droplets. Yet, relying on jetting for droplet production comes with inherent challenges.

In the jetting regime, we observe a sizable amount of polydispersity in the droplets formed after one line of glycerol is deposited in the bath. The distance between these drops follows a distribution centered on λ_m with a standard deviation nearing 15% of λ_m [41]. Such a sizable difference in droplet distance (and thus droplet size) is due to the convective nature of the instability [10]. The system's noise is progressively amplified following the dispersion relation, which is quite flat around the max: a change in the value of k of nearly 15% merely decreases σ by 1% (see Fig. 5). Many modes are thus amplified and combined to create droplets of variable sizes. Yet, when depositing threads next to one another sequentially, we find that polydispersity progressively diminishes [Fig. 5(b)]. This effect is only apparent if the successive lines are deposited near each other [41].

To rationalize the ability of the RPI to self-correct in the above-described scenario, we move to extrude threads of glycerol near a corrugated boundary with wavelength λ_m and study the evolution of the droplets' polydispersity with δ, the distance from the jet to the template [Fig. 5(c)]. We find a cutoff distance to the template under which drops are monodisperse and above which the system's natural tendency to produce polydisperse drops slowly resurfaces. This cutoff value depends solely on the thread size and is about $\delta = 8h_0$. Additionally, we find that the jet length ℓ_j decreases when close to the boundary. Shorter jets mean that the drops are forming faster. Yet, the growth rate of the instability remains unchanged [41]. These findings suggest that the initial amplitude ϵ of the perturbations increases when printing close to the template. In practice, we indirectly measure ϵ combining the breakup time, ℓ_j/U_0 and the empirical criteria $\epsilon e^{\sigma \ell_j/U_0} \simeq h_0$ to find

$$\epsilon/h_0 \propto \exp(-\delta/h_0), \tag{11}$$

although we can offer no detailed explanation for this expression. Equation (11) indicates that templates merely modify the problem's initial conditions. These monochromatic perturbations are set to match the RPI's most unstable mode, and grow unchallenged, thereby reducing the drops' heterogeneity.

These results suggest that it is theoretically possible to force the Rayleigh-Plateau away from its most unstable mode by tailoring initial perturbations with a large enough amplitude and a wavelength λ that differs from λ_m. With this strategy, one can lock in the breakup to the template in a wavelength range $0.6\lambda_m < \lambda < 1.4\lambda_m$ [41]. Beyond this range, we recover λ_m regardless of the value of λ.

This last result helps rationalize the self-correction of the droplets' distribution when successive lines are printed: large defects in the droplet lattice, i.e., where the distance between drops is larger (resp. smaller) than $1.4\lambda_m$ (resp. $0.6\ \lambda_m$), disappear at the following line. Any other pair of drops leads to the formation of a single drop. The distance between two newly formed daughter drops can be estimated as the average distance between the mother drops. The system behaves like a moving average, smoothing an initially noisy signal oscillating around a mean value. This mean value, λ_m, is obtained virtually free of any oscillations after a few lines are printed [see inset in Fig. 5(a)].

We note that drops produced in these experiments tend to move after they are formed. The motion of the nozzle necessary to print subsequent lines generates a flow in the bath a flow, which, in turn, drags existing drops in the same direction. The displacement of the drops is indexed on the speed of the nozzle U_0, while their size depends on U_i/U_0. Maintaining this ratio constant while varying U_0 allows the creation of regular lattices with tunable geometry [41]. Using templates allows different drops of different sizes to coexist in the same lattice [Fig. 5(d)], thereby allowing a wealth of patterns to be formed and carefully tuned.

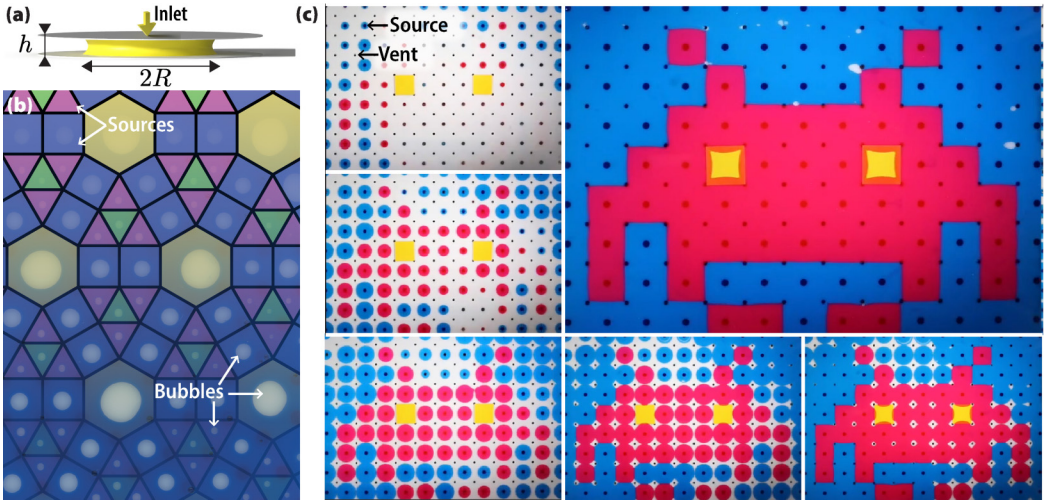

FIG. 6. (a) Schematic of the working principle from Ref. [47]. A hole in the top plate of a Hele-Shaw cell allows the cell to wick the liquid. (b) Photograph of a sample obtained using a regular tiling of sources. (c) Progressive invasion of colored polymers through a network of sources. The vents remove any air bubbles trapped where the flows meet.

IV. STABLE CAPILLARY FLOWS

Interfacial flows, in their stable limit, are widely used in the laboratory and industry [11]. Of particular interest for these applications is that capillary effects produce smooth surfaces. For instance, such ability is an asset when assembling objects requiring optical qualities. Capillary effects have long been used to shape glass in the float process [44]. More recently, curved optical components with complex geometries have been demonstrated using interfacial effects in neutrally buoyant conditions [45] or space [46]. Capillary and viscous effects are also crucial in setting the thickness of coatings, in spin coating and in dip coating [21]. In this section, we discuss two variants of these classic problems, which showcase the robustness and programmability of interfacial flows.

A. Capillary suction

We explore a strategy for assembling patterns based on capillary suction. These flows oringinate from a distribution of point sources [47]. This approach is formally akin to the watershed transform and relies on interfacial flows similar to the capillary rise to generate motion. Here, we consider the case of a wetting liquid placed between two horizontal plates with spacing h (Fig. 6). The interface curvature is of the order of $2/h$, creating a pressure difference of $2\gamma/h$ with the surrounding atmosphere. This liquid is connected to a pool by a small aperture in the top plate, such that there is a pressure gradient $2\gamma(hR)^{-1}$ between the center of the liquid and its boundary, with R the size of the puddle. This gradient is resisted by viscous dissipation $\mu\frac{dR}{dt}h^{-2}$, yielding $R \propto \sqrt{t}$, similar to Washburn law [21]. Since gravity is unimportant here, the flow could go uninterrupted. In practice, the flow is eventually stopped for two reasons.

First, we use a liquid elastomer that cures in finite time τ_c per Eq. (4). We thus find the existence of a maximum attainable radius R_∞[47]:

$$R_\infty = \sqrt{\frac{R_0^2 + \gamma h \tau_c \cos\theta}{9\mu_0}}. \tag{12}$$

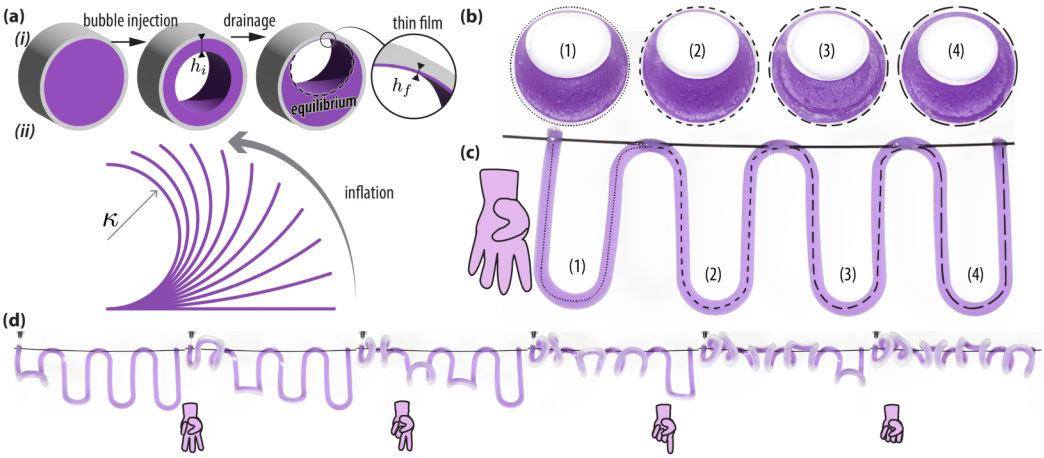

FIG. 7. (a) (i) Bubble casting involves the injection of a bubble to carve a cavity with rim thickness h_i, which then drains to leave a thin film with thickness h_f at the top of the sample. (ii) Shape morphing that follows inflation of the sample [49]. (b) Photographs demonstrate the film thickness change through Eq. (15). Areas from (1) to (4) have an increasing value of the work time τ_w and thus an increasing film thickness h_f. (c) Handlike actuator whose inflation yields (d) a sequential motion of each digit from (1) to (4) while the pressure in the sample is continuously increased.

Second, we typically work with multiple flows originating from a collection of source points separated by a distance $d < 2R_\infty$. As such, there exists a time when the flows from each source meet, thereby annihilating the liquid-air interface. Rapid coalescence is observed due to the sizable planar curvature that forms at this singular point. Bubbles are trapped when three or more flows merge. Regular tilings of sources lead to regular arrays of air bubbles, whose area increase with the number of sides of the tile [Fig. 6(b)].

Trapped bubbles can be suppressed by placing vents [47]. Interestingly, in this form, the liquid originating from each source fills the region of the plane closest to the source, thus forming a Voronoi diagram when the sources are close enough [see Fig. 6(c)]. More complex source shapes, e.g., rectangles, form patterns corresponding to their distance transform. Complex tesselations can be obtained simply by tuning the positions and shapes of the sources.

There are many possible generalizations to this problem: cases where the viscosity of the polymer varies from source to source, cases where the liquids are introduced at different times [47], or even cases where entirely different mechanisms drive the invasion as in cell proliferation [48].

After polymerization is complete, the planar assemblies formed by these capillary flows are elastic sheets with properties varying across the sample and entirely defined by the geometry of the sources. Altering the sheet's mechanical properties yields programmable materials that can morph into specific shapes when inflated [47].

B. Drainage of a thin film

In this last section, we explore a fabrication methodology that leverages the drainage of a thin coating to enable the assembly and programming of a soft robotic actuator. This approach, called bubble casting [49], relies on injecting an elongated air bubble into a tubular mold, initially loaded with an uncured liquid elastomer. This Bretherton-like flow leaves a rim with thickness h_i [see Fig. 7(a)]. In such a flow, the viscous dissipation and the capillary pressure gradient write $\mu U/h_i^2$ and $\gamma/((R-h_i)\ell)$. Here, ℓ is *a priori* unknown length scale determined by the curvature $1/(R-h_i) \simeq h_i/\ell^2$. Balancing those terms yields $h_i \simeq (R-h_i)\mathrm{Ca}^{2/3}$, with $\mathrm{Ca} = \mu U/\gamma$, the capillary number. A

more thorough analysis [50] reveals that

$$h_i = R\frac{1.34\mathrm{Ca}^{2/3}}{1 + 2.65 \times 1.34\mathrm{Ca}^{2/3}}. \tag{13}$$

In the immediate aftermath of this coating, the deposited film drains. For Newtonian liquids, an exact solution can be derived at the apex [51]:

$$h = \frac{h_i}{\sqrt{1 + \frac{2}{3}\frac{\rho g h_i^2}{\mu R}t}}. \tag{14}$$

Performing a nonlinear expansion of Eq. (14) shows little variation of the thickness with the azimuthal angle [52]. The film at the top of the sample is virtually uniform [Fig. 7(a)]. Additionally, in the limit of large times, $t \gg \mu R/(\rho g h_i^2)$, Eq. (14) becomes independent of h_i; $h \simeq \sqrt{\frac{3\mu R}{2\rho g t}}$. When working with elastomers, one needs to account for the evolution of the viscosity during curing. Using Eq. (4), we obtain

$$h_\mathrm{f} = 3\sqrt{\frac{\mu_0 R}{2\rho g \tau_c}\left(\frac{\tau_c}{\tau_c - \tau_w}\right)^3}, \tag{15}$$

where τ_c is the curing time and τ_w the work time when the bubble is injected. This thin film matches the lower part of the sample, whose shape follows the Young-Laplace equation in two dimensions [49] [see the equilibrium shape in Fig. 7(a)].

The unique solution corresponding to a particular experiment is found by evaluating the void fraction $\phi = (1 - \frac{h_i}{R})^2$ determined by Eq. (13).

Equations (13) and (15) have practical consequences, which are worth commenting here. We note that h_i is nearly constant with $h_i \simeq 0.3\,R$ in the range of Ca explored, yielding $\phi \simeq 0.5$. The amount of fluid left by bubble casting is robust and does not require precise control of the flow rate. Another critical element is that the thickness of the film h_f as predicted in Eq. (15) is invariant across the sample so long that variations in work time are small compared to the curing time $\Delta\tau_w \ll \tau_c$. In practice, we produced meter-long samples with nearly uniform submillimeter films [49]. However, purposefully choosing significantly different values of τ_w across a sample allows for locally dictating the value of h_f [see Fig. 7(b)].

In summary, the results in this section enable the assembly of monolithic tubes with carefully crafted and anisotropic cross-sections, comprising a thin film at their top and a croissantlike shape at their bottom. In turn, these samples can be pressurized after curing is complete. Upon inflation, the thin part of the sample deforms more than the thicker region, forcing an out-of-plane deformation [see Fig. 7(a)]. The curvature, κ, of the newly formed elastic rod is locally dictated by

$$\kappa R = \left(\frac{P}{G}\right)^\alpha \left(\frac{R}{h_\mathrm{f}}\right)^{\alpha-1}, \tag{16}$$

where P is the applied pressure, G the cured polymer shear modulus, and $\alpha \simeq 3.7$ is a coefficient obtained by fitting experiments to an Ansatz that follows from dimensional analysis [49]. Equation (16) highlights the interplay between fluid dynamics and elasticity. The mechanical property of the actuator is sensitive to the value of the film thickness, which, all things being equal, can be tuned by timing the bubble injection [see Eq. (15)]. It is possible to create actuators whose response to a monotonic pressure increase will be a sequential series of elastic deformations [Figs. 7(c) and 7(d)], paving the way for developing programmable shape morphing materials for applications in soft robotics and other connected fields.

V. CONCLUSION

This article demonstrates that interfacial flows can be leveraged to assemble complex structures precisely. These efforts are in continuity with what has long been done in specific fields, e.g., atomization, microfluidics, coatings, and other industrial processes that rely on surface tension. This article provides additional insights on taming these flows. It points out the necessity to study pattern formation further from the threshold of their appearance and devise strategies for their control, e.g., via seeds. The questions of patterns's growth and the amount of memory carried or erased in these systems remain largely open. When it comes to memory, both limits have value. Universal shapes arise when memory is suppressed. Those shapes are inherently robust, suggesting little control is needed for their formation. Conversely, keeping some memory of initial or boundary conditions allows control, which is appreciable when solving the inverse design problem to reach a target shape.

This article also highlights the importance of further studying and understanding the interplay between flow and solidification [53,54]. Equation (4) is particularly simple, more efforts will be required to generalize these approaches to a broader range of liquids, including epoxies, foams, glass [55], and concrete. For those, time or space-varying viscosity might contribute to pattern formation [53], and shear or similar effects could be used to align suspended particles and achieve hierarchical structures [56,57].

Finally, there is a vibrant research community that lives at the intersection of soft matter physics, solid mechanics, and material science, whose contributions go far beyond what was discussed in this article (for example, in Refs. [58–61]). In particular, we note that the role of fluid flows in biological systems has been widely reported in the formation and function of membraneless compartments in living cells [62]. Inspired by the relevance of surface tension and interfacial flows in the life of many organisms, we, as others, aim to transpose these phenomena into artificial laboratory settings and demonstrate that analogous principles can be leveraged to engineer soft materials exhibiting augmented functionalities.

ACKNOWLEDGMENTS

I want to thank the Liquid and Elasticity Laboratory (LE. Lab) group members, past and present, for their continuous efforts to make this work possible. I also want to thank François Gallaire for helpful conversations. This work was supported by the NSF CAREER award (CBET 2042930) and the NSF FMRG award (CMMI 2037097).

[1] J. D. Currey, *Bones: Structure and Mechanics* (Princeton University Press, Princeton, NJ, 2002).

[2] D. Quéré and M. Reyssat, Non-adhesive lotus and other hydrophobic materials, Philos. Trans. R. Soc. A **366**, 1539 (2008).

[3] S. Kinoshita and S. Yoshioka, Structural colors in nature: The role of regularity and irregularity in the structure, ChemPhysChem **6**, 1442 (2005).

[4] J. Teyssier, S. V. Saenko, D. Van Der Marel, and M. C. Milinkovitch, Photonic crystals cause active colour change in chameleons, Nat. Commun. **6**, 6368 (2015).

[5] N. I. Zheludev and Y. S. Kivshar, From metamaterials to metadevices, Nat. Mater. **11**, 917 (2012).

[6] S. A. Cummer, J. Christensen, and A. Alù, Controlling sound with acoustic metamaterials, Nat. Rev. Mater. **1**, 16001 (2016).

[7] K. Bertoldi, V. Vitelli, J. Christensen, and M. Van Hecke, Flexible mechanical metamaterials, Nat. Rev. Mater. **2**, 17066 (2017).

[8] P. M. Reis, A perspective on the revival of structural (in) stability with novel opportunities for function: From buckliphobia to buckliphilia, J. Appl. Mech. **82**, 111001 (2015).

[9] X. Xia, C. M. Spadaccini, and J. R. Greer, Responsive materials architected in space and time, Nat. Rev. Mater. **7**, 683 (2022).
[10] F. Gallaire and P.-T. Brun, Fluid dynamic instabilities: Theory and application to pattern forming in complex media, Philos. Trans. R. Soc. A **375**, 20160155 (2017).
[11] P.-T. Brun, Fluid-mediated fabrication of complex assemblies, JACS Au **2**, 2417 (2022).
[12] D. W. Thompson, in *On Growth and Form*, edited by J. T. Bonner and Canto (Cambridge University Press, Cambridge, England, 1992).
[13] F. Charru, B. Andreotti, and P. Claudin, Sand ripples and dunes, Annu. Rev. Fluid Mech. **45**, 469 (2013).
[14] L. Goehring and S. W. Morris, Cracking mud, freezing dirt, and breaking rocks, Phys. Today **67**, 39 (2014).
[15] D. Quéré, Fluid coating on a fiber, Annu. Rev. Fluid Mech. **31**, 347 (1999).
[16] R. E. Rosensweig, *Ferrohydrodynamics* (Courier Corporation, North Chelmsford, MA, 1997).
[17] G. I. Taylor, The instability of liquid surfaces when accelerated in a direction perpendicular to their planes. I, Proc. R. Soc. London A **201**, 192 (1950).
[18] D. H. Sharp, An overview of Rayleigh-Taylor instability, Physica D **12**, 3 (1984).
[19] M. Fermigier, L. Limat, J. E. Wesfreid, P. Boudinet, and C. Quilliet, Two-dimensional patterns in Rayleigh-Taylor instability of a thin layer, J. Fluid Mech. **236**, 349 (1992).
[20] J. Marthelot, E. F. Strong, P. M. Reis, and P.-T. Brun, Designing soft materials with interfacial instabilities in liquid films, Nat. Commun. **9**, 4477 (2018).
[21] P.-G. Gennes, F. Brochard-Wyart, and D. Quéré, *Capillarity and Wetting Phenomena: Drops, Bubbles, Pearls, Waves* (Springer, New York, 2004).
[22] P.-T. Brun, A. Damiano, P. Rieu, G. Balestra, and F. Gallaire, Rayleigh-Taylor instability under an inclined plane, Phys. Fluids **27**, 084107 (2015).
[23] P. G. Ledda, G. Lerisson, G. Balestra, and F. Gallaire, Instability of a thin viscous film flowing under an inclined substrate: The emergence and stability of rivulets, J. Fluid Mech. **904**, A23 (2020).
[24] P. H. Trinh, H. Kim, N. Hammoud, P. D. Howell, S. J. Chapman, and H. A. Stone, Curvature suppresses the Rayleigh-Taylor instability, Phys. Fluids **26**, 051704 (2014).
[25] G. Balestra, N. Kofman, P.-T. Brun, B. Scheid, and F. Gallaire, Three-dimensional Rayleigh–Taylor instability under a unidirectional curved substrate, J. Fluid Mech. **837**, 19 (2018).
[26] G. Balestra, D. M.-P. Nguyen, and F. Gallaire, Rayleigh-Taylor instability under a spherical substrate, Phys. Rev. Fluids **3**, 084005 (2018).
[27] E. Jambon-Puillet, M. R. Piéchaud, and P.-T. Brun, Elastic amplification of the Rayleigh–Taylor instability in solidifying melts, Proc. Natl. Acad. Sci. USA **118**, e2020701118 (2021).
[28] V. Lapuerta, F. J. Mancebo, and J. M. Vega, Control of Rayleigh-Taylor instability by vertical vibration in large aspect ratio containers, Phys. Rev. E **64**, 016318 (2001).
[29] B. Venkateswaran, T. J. Jones, G. Kresge, J. Marthelot, E. Jambon-Puillet, and P.-T. Brun, Stacked Rayleigh-Taylor instabilities grow drops into soft stalactite-like structures, arXiv:2403.09837.
[30] J. R. Lister, J. M. Rallison, and S. J. Rees, The nonlinear dynamics of pendent drops on a thin film coating the underside of a ceiling, J. Fluid Mech. **647**, 239 (2010).
[31] E. Jambon-Puillet, P. G. Ledda, F. Gallaire, and P.-T. Brun, Drops on the underside of a slightly inclined wet substrate move too fast to grow, Phys. Rev. Lett. **127**, 044503 (2021).
[32] J. Eggers and E. Villermaux, Physics of liquid jets, Rep. Prog. Phys. **71**, 036601 (2008).
[33] A. S. Utada, A. Fernandez-Nieves, H. A. Stone, and D. A. Weitz, Dripping to jetting transitions in coflowing liquid streams, Phys. Rev. Lett. **99**, 094502 (2007).
[34] J. K. Nunes, S. S. H. Tsai, J. Wan, and H. A. Stone, Dripping and jetting in microfluidic multiphase flows applied to particle and fibre synthesis, J. Phys. D **46**, 114002 (2013).
[35] C. N. Baroud, F. Gallaire, and R. Dangla, Dynamics of microfluidic droplets, Lab Chip **10**, 2032 (2010).
[36] A. R. Studart, H. C. Shum, and D. A. Weitz, Arrested coalescence of particle-coated droplets into nonspherical supracolloidal structures, J. Phys. Chem. B **113**, 3914 (2009).
[37] H. A. Stone and M. P. Brenner, Note on the capillary thread instability for fluids of equal viscosities, J. Fluid Mech. **318**, 373 (1996).

[38] S. Tomotika, On the instability of a cylindrical thread of a viscous liquid surrounded by another viscous fluid, Proc. R. Soc. London A **150**, 322 (1935).
[39] A. Javadi, J. Eggers, D. Bonn, M. Habibi, and N. M. Ribe, Delayed capillary breakup of falling viscous Jets, Phys. Rev. Lett. **110**, 144501 (2013).
[40] L. Cai, J. Marthelot, and P.-T. Brun, An unbounded approach to microfluidics using the Rayleigh–Plateau instability of viscous threads directly drawn in a bath, Proc. Natl. Acad. Sci. USA **116**, 22966 (2019).
[41] L. Cai, J. Marthelot, and P.-T. Brun, Instability mediated self-templating of drop crystals, Sci. Adv. **8**, eabq0828 (2022).
[42] L. Cai, J. Marthelot, C. Falcón, P. M. Reis, and P.-T. Brun, Printing on liquid elastomers, Soft Matter **16**, 3137 (2020).
[43] J. Eggers, Drop formation–an overview, Z. Angew. Math. Mech. **85**, 400 (2005).
[44] L. A. Bethune Pilkington, Review lecture: The float glass process, Proc. R. Soc. London A **314**, 1 (1969).
[45] V. Frumkin and M. Bercovici, Fluidic shaping of optical components, Flow **1**, E2 (2021).
[46] O. Luria, M. Elgarisi, V. Frumkin, A. Razin, J. Ericson, K. Gommed, D. Widerker, I. Gabay, R. Belikov, and J. Bookbinder, Fluidic shaping and in-situ measurement of liquid lenses in microgravity, npj Microgr. **9**, 74 (2023).
[47] M. Badaoui, G. Kresge, C. Ushay, J. Marthelot, and P.-T. Brun, Formation of pixelated elastic films via capillary suction of curable elastomers in templated Hele–Shaw cells, Adv. Mater. **34**, 2109682 (2022).
[48] M. A. Heinrich, R. Alert, A. E. Wolf, A. Košmrlj, and D. J. Cohen, Self-assembly of tessellated tissue sheets by expansion and collision, Nat. Commun. **13**, 4026 (2022).
[49] T. J. Jones, E. Jambon-Puillet, J. Marthelot, and P.-T. Brun, Bubble casting soft robotics, Nature (London) **599**, 229 (2021).
[50] P. Aussillous and D. Quéré, Quick deposition of a fluid on the wall of a tube, Phys. Fluids **12**, 2367 (2000).
[51] D. Takagi and H. E. Huppert, Flow and instability of thin films on a cylinder and sphere, J. Fluid Mech. **647**, 221 (2010).
[52] A. Lee, P.-T. Brun, J. Marthelot, G. Balestra, F. Gallaire, and P. M. Reis, Fabrication of slender elastic shells by the coating of curved surfaces, Nat. Commun. **7**, 11155 (2016).
[53] S. Mowlavi, I. Shukla, P.-T. Brun, and F. Gallaire, Particle size selection in capillary instability of locally heated coaxial fiber, Phys. Rev. Fluids **4**, 064003 (2019).
[54] T. F. Yap, A. Rajappan, M. D. Bell, R. M. Rasheed, C. J. Decker, and D. J. Preston, Thermally accelerated curing of platinum-catalyzed elastomers, Cell Rep. Phys. Sci. **5**, 101849 (2024).
[55] P.-T. Brun, C. Inamura, D. Lizardo, G. Franchin, M. Stern, P. Houk, and N. Oxman, The molten glass sewing machine, Philos. Trans. R. Soc. A **375**, 20160156 (2017).
[56] C. Zhao, P. Zhang, J. Zhou, S. Qi, Y. Yamauchi, R. Shi, R. Fang, Y. Ishida, S. Wang, and A. P. Tomsia, Layered nanocomposites by shear-flow-induced alignment of nanosheets, Nature (London) **580**, 210 (2020).
[57] D. Nepal, S. Kang, K. M. Adstedt, K. Kanhaiya, M. R. Bockstaller, L. C. Brinson, M. J. Buehler, P. V. Coveney, K. Dayal, and J. A. El-Awady, Hierarchically structured bioinspired nanocomposites, Nat. Mater. **22**, 18 (2023).
[58] A. Z. Nelson, B. Kundukad, W. K. Wong, S. A. Khan, and P. S. Doyle, Embedded droplet printing in yield-stress fluids, Proc. Natl. Acad. Sci. USA **117**, 5671 (2020).
[59] F. J. Dent, D. Harbottle, N. J. Warren, and S. Khodaparast, Temporally arrested breath figure, ACS Appl. Mater. Interfaces **14**, 27435 (2022).
[60] J. J. Kaufman, G. Tao, S. Shabahang, E.-H. Banaei, D. S. Deng, X. Liang, S. G. Johnson, Y. Fink, and A. F. Abouraddy, Structured spheres generated by an in-fibre fluid instability, Nature (London) **487**, 463 (2012).
[61] A. Gumennik, L. Wei, G. Lestoquoy, A. M. Stolyarov, X. Jia, P. H. Rekemeyer, M. J. Smith, X. Liang, B. J.-B. Grena, and S. G. Johnson, Silicon-in-silica spheres via axial thermal gradient in-fibre capillary instabilities, Nat. Commun. **4**, 2216 (2013).
[62] B. Gouveia, Y. Kim, J. W. Shaevitz, S. Petry, H. A. Stone, and C. P. Brangwynne, Capillary forces generated by biomolecular condensates, Nature (London) **609**, 255 (2022).